Snowmelt as a determinant factor in the hydrogeological behavior of high mountain karst aquifers: The Garcés karst system, Central Pyrenees (Spain).

Jódar, J. [a,*], González-Ramón, A.[a], Martos-Rosillo, S.[a], Heredia, J.[a], Herrera, C.[b], Urrutia, J.[c], Caballero, Y.[d], Zabaleta, A.[e], Antigüedad, I.[e], Custodio, E.[f], Lambán, L.J.[a]

(a) Geological and Mining Institute of Spain (IGME), Spain

(b) Universidad Bernardo O'Higgins, Centro de Investigación y Desarrollo de Ecosistemas Hídricos, Santiago, Chile

(c) Department of Mining Engineering, Antofagasta University, Antofagasta, Chile

(d) French Geological Survey, France

(e) Hydro-Environmental Processes Group, Science and Technology Faculty, University of the Basque Country UPV/EHU, Leioa, 48940, Basque Country, Spain

(f) Groundwater Hydrology Group, Department of Civil and Environmental Engineering, Technical University of Catalonia (UPC) & Royal Academy of Sciences of Spain, Spain

(*) Corresponding author: J. Jódar, C/ Manuel Lasala, 44. 9ºB, 50006, Zaragoza. Spain. (j.jodar@igme.es). Tlf: +34-619712122

Abstract

Time series of environmental tracers (groundwater stable isotope composition, electrical conductivity and temperature) and concentration breakthrough curves of artificial tracers (uranine, eosine, amino-G and naphtionate) were analyzed to characterize fast preferential and slow matrix in-transit recharge flows in the Paleocene-Eocene limestone aquifer of the Ordesa and Monte Perdido National Park. This is an alpine karst system drained by a water-table cave, a rare hydrological feature in high mountain karst systems with similar characteristics. Snowmelt favors the areal recharge of the system. This process is reflected in the large proportion of groundwater flowing through the connected porosity structure of the karst aquifer, which amounts the 75% of the total system water discharge. From the perspective of water resources recovery, the water capacity of the fissured-porous zone (matrix) represents 99% of the total karst system storage. The volume associated to the karst conduits is very small. The estimated mean transit times are 9 days for conduits and 475 days for connected porosity. The short transit times, even the longer ones, mean high vulnerability of the karst system to contaminants and great impact of climate change.

Key words: Water isotopes; Dye tracers; Transit time; Recharge; Alpine karst hydrology; Parque Nacional de Ordesa y Monte Perdido.

1. Introduction

High mountain zones are known as "water towers" because they generate the main water resources feeding the lowland depending ecosystems (Viviroli et al., 2007). When these mountains constitute or host an aquifer, then the collected water resources remain in the basin for a longer time, because aquifers regulate the basin discharge. Thus, mountain aquifers provide a strategic water resource in dry seasons, especially in semi-arid regions. From the perspective of water resources availability, carbonated aquifers are those arousing the most interest as they represent 15.2% of the land surface and provide drinking water to about 10% of the world’s population (Stevanovic, 2019). Globally, 31.1% of all the surface exposures of carbonate rocks occur in plains, whereas 68.9% do in hills and mountain zones (Goldscheider et al., 2020).

A good characterization of the karst system behavior is essential to manage correctly aquifer discharge. The hydrodynamical response of karst aquifers greatly depends both on the type of recharge and on their underground geological structure (Audra and Palmer, 2011: 2015). On the one hand, when the aquifer recharge is uneven and occurring quickly with high flow rates, the hydrodynamical perturbation propagates through the system and generates flash discharges. As a result, the epiphreatic zone experiences often back flooding events with dry periods in between, thus developing drains with looping profiles. An example is the Hollock cave (Bögli, 1980), one of the most extensive limestone caves currently known, which is developed inside the alpine Austro-German Hochifen-Gottesacker karst system (Goldscheider, 2005; Göppert and Goldscheider 2008; Chen and Goldscheider 2014). On the other hand, when recharge enters the system in a diffuse and regular way as a consequence of a poorly permeable surface cover over the epikarst, then the aquifer water table remains fairly stable with time, and the principal drain of the system, also known as water table cave, develops at the water table level, as it happens in the Cobre cave system in the Cantabrian Mountains (Rossi et al., 1997).

In high mountain zones, where the snow covers the ground surface during long periods or even the whole year, the thaw may produce a diffuse recharge process in the underlying karst systems (Meeks and Hunkeler, 2015). This process, that would emulate the role played by the aforementioned permeable soil cover, may be also very important in glacierized catchments, although only a few researchers have studied the relations between alpine glaciers and the underlaying karst aquifers (Smart, 1996; Gremaud et al. 2009; Zheng et al. 2015). Diffuse recharge may favor small changes in elevation of the water table, which is an essential condition for the development of horizontal cave passages (Gabrovsek and Dreybrodt, 2001; Kaufmann 2002). Nevertheless, the role played by snow accretion and melting dynamics in high mountain karst aquifers in relation to the development of cave patterns is little known. In fact, many of the studies in this regard have been carried out in caves whose recharge areas are below 2000 m a.s.l. (Häuselmann, 2019), up to an elevation in which rainfall infiltration dynamics dominates recharge. As a result, most of the described caves present a looping cave pattern. The very few geomorphological descriptions of water-table caves developed in high mountain zones reflect the difficulties inherent to the exploration activities imposed by the harsh working conditions in high elevation alpine zones.

This work is devoted to characterize the hydrogeological behavior of the alpine Garcés water table cave and the associated bare karst system that are developed at elevations between 2000 and 3300 m a.s.l.. The characterization is conducted through a multidisciplinary approach that includes physicochemical and hydrological monitoring of the karst system discharge, and the use of environmental and fluorescent dye tracers testing techniques. The Garcés water table cave drains the highest aquifer karst in Western Europe, the alpine Paleocene-Eocene limestones of the Ordesa and Monte Perdido National Park, in the Central Southern sector of the Pyrenees. The terminal point of the Garcés cave is the Garcés spring, whose discharge generates the known Cola de Caballo (*Water Horsetail*) waterfall and highlights the significant natural heritage value of the study zone (Ortega-Becerril et al., 2019).

2. The study area

2.1 Geographical and climatic settings

The study area is located in the Ordesa and Monte Perdido National Park (PNOMP from the initials in Spanish), in the Central-Southern Pyrenees (Fig. 1). The PNOMP constitutes the highest karst system in Western Europe. It contains several peaks above 3000 m a.s.l. The Monte Perdido (3348 m a.s.l.) is its highest point.

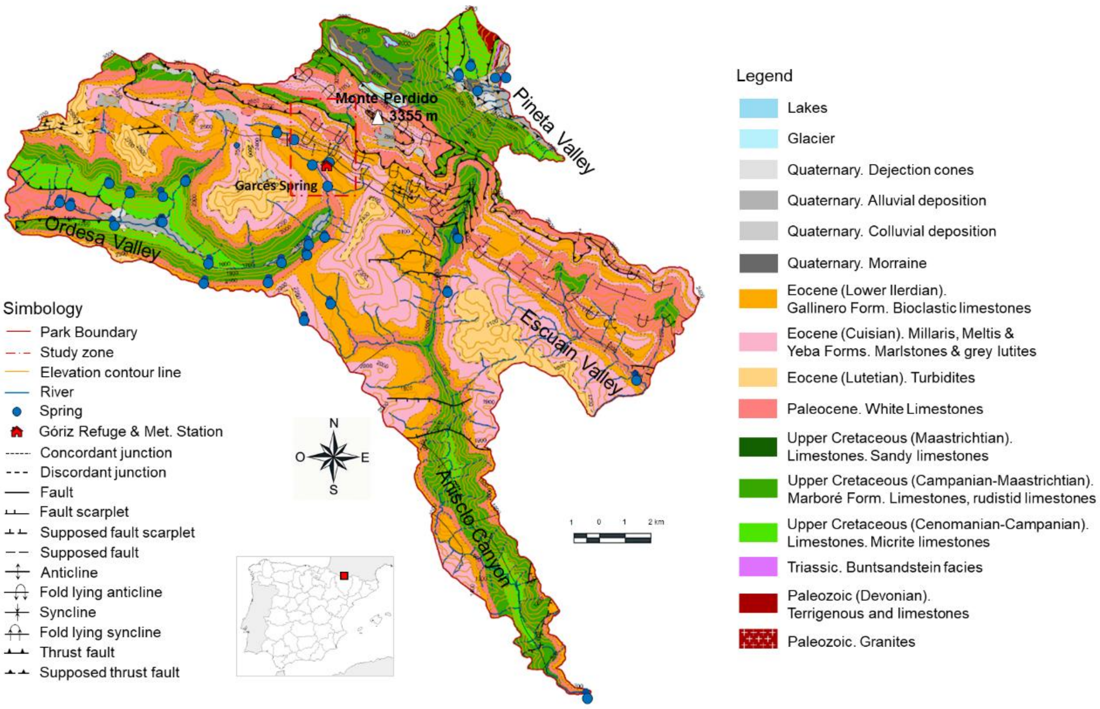

Fig. 1. Geological map of the the Ordesa and Monte Perdido National Park (PNOMP). The study zone is indicated by the red dashed line. Modified from Lambán et al. (2015).

The PNOMP has a cold climate with mild and cool summers (AEMET/IM, 2011). The main precipitation (P) volumes registered in the PNOMP are generated by oceanic low pressure fronts arriving from the Atlantic Ocean (Lambán et al., 2015). The study area is covered by snow between October and June. The mean annual precipitation at the Góriz Meteorological station (Fig. 1, at 2200 m a.s.l.) is 1650 mm (Fig. 2). Precipitation (P) presents two peaks in autumn and spring, at 221 and 178 mm/month, respectively, and two minima in winter and summer, at 87 and 104 mm/month, respectively. At the same meteorological station the air temperature (T_{2m}) shows a seasonal evolution with maximum and minimum monthly averaged values of 13°C (July) and -0.6°C

(December), respectively (Fig. 2). The mean annual temperature is 4.9 °C. Both P and T_{2m} present significant altitudinal variations in the area, with mean vertical gradients of P and T_{2m} of 200 mm/km and -3.3 °C/km, respectively (Lambán et al., 2015).

The mean isotopic content of precipitation (δ_P) in the PNOMP shows a seasonal variation, as does the T_{2m}. The mean annual value of $\delta^{18}O$ (δ_P) in the meteorological station of Góriz is -11.25‰, and the mean amplitude (A_δ) is 4.97‰. Besides, δ_P and A_δ vary with elevation, with altitudinal slopes of −2.2‰/km and 0.9‰/km, respectively (Jódar et al., 2016b).

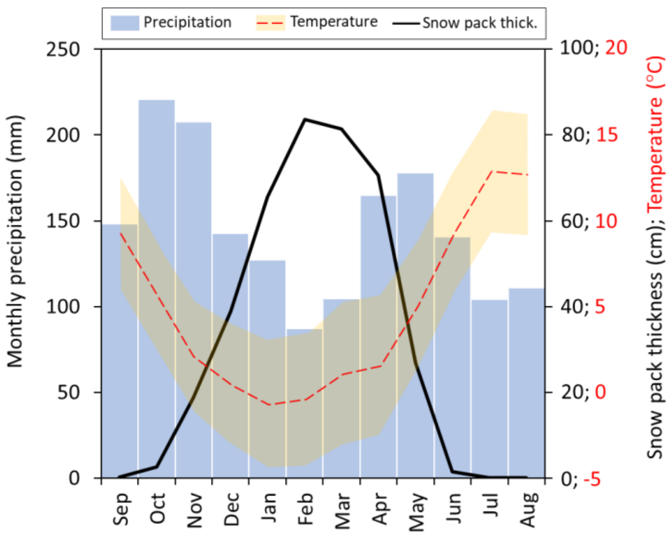

Fig. 2. Seasonal variation of average monthly precipitation (columns), soil accumulated snow pack thickness (thick line), and monthly average air temperature (dashed line) with the corresponding maximum and minimum values marked as a variation interval (shaded area) at the meteorological station of Góriz (2220 m a.s.l.), for the period 1981-2019

2.2 Geological and hydrogeological settings

The PNOMP is located in the central-western sector of the southern Pyrenees, forming part of the Sierras Interiores (*Inner Ranges*) structural unit. Its geological structure is characterized by imbricated thrust sheets and associated folds of carbonate materials, with a predominantly southern vergence (Séguret, 1972). The age of the different materials composing the massif ranges from Upper Cretaceous (Marboré Formation) to the Lower Paleocene-Eocene (Gallinero Formation) (Lambán et. al., 2015; Robador et. al., 2018). The layout of the different materials by stacking several thrust sheets generates a vertical development close to 1000 m from the Marboré peak to the Garcés Spring (Fig 3).

The limestones associated to the Gallinero Formation are karstified and constitute the main aquifer drained by the Garcés Spring. The calcareous Paleocene-Eocene materials and their vertical disposition favor both the karstification process and the existence a very thick unsaturated zone due to an imbricated group of overthrust sheets and associated folds. The base of the karst aquifer is the low permeability materials of the Marboré Formation (calcareous sandstone with intercalations of both quartz and lithic arenites).

The karst system is subject of active exploration so far with the aim of proving the hydrological connection between the different mapped galleries (Fig.3A). The karst exploration has revealed that the network in the vadose zone is of the branchwork type (Jouves et al., 2017), which is the most frequent development pattern in mountainous karst massifs. In the epiphreatic zone, the karst development pattern type is of the water table cave type. This pattern is associated with diffuse recharge processes, which often involves a well-developed epikarst zone or a semi-confining layer that covers the deeper most permeable materials. Nevertheless, a well-developed epikarst or a surficial semi-confining layer do not exist in the study area

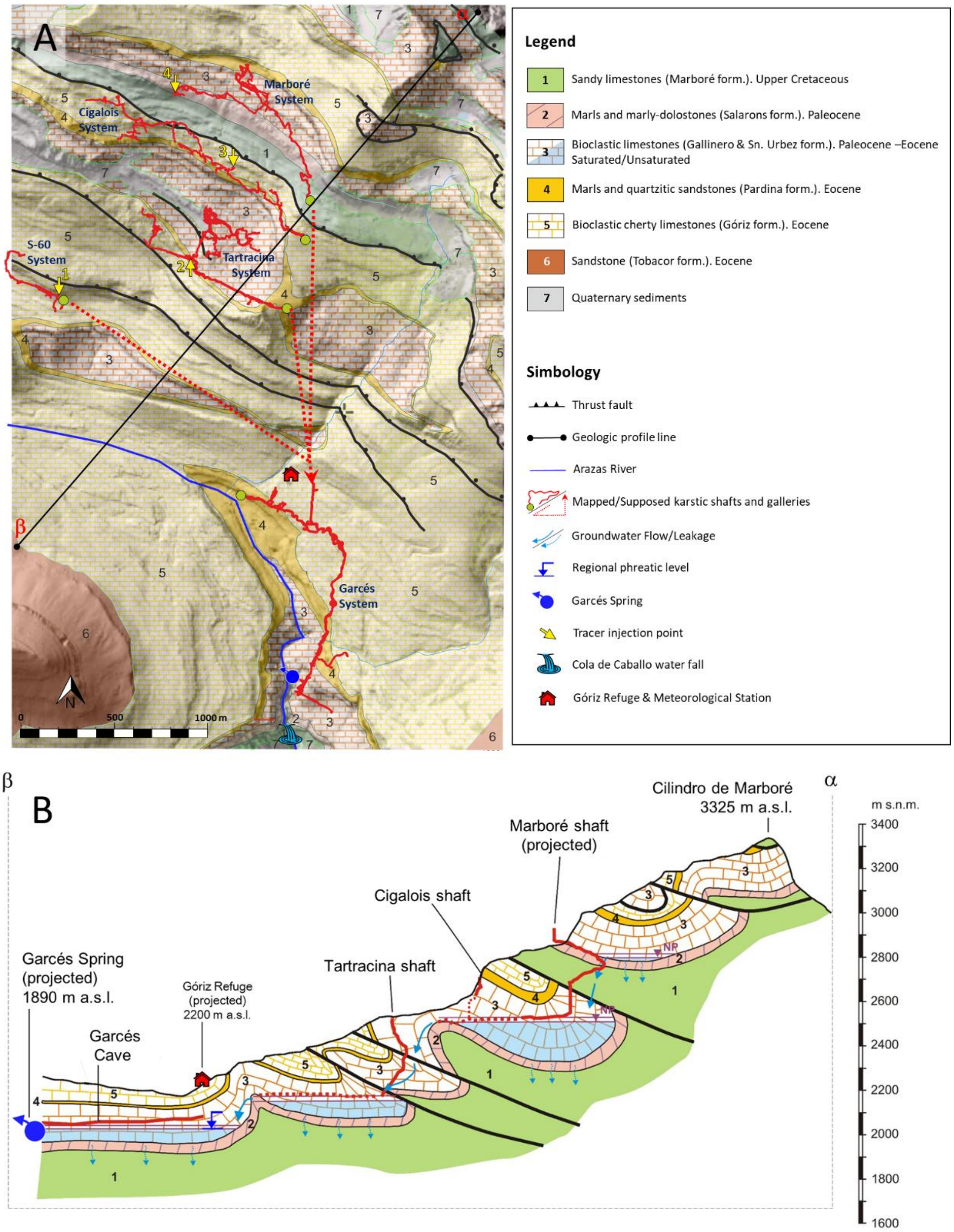

Fig. 3. Hydrogeological conditions. (A) Hydrogeological map of the study zone. The main karst cave systems of the area are marked in red. Most of them have not been completely explored. The green circle indicates the terminal sump of the corresponding karst systems. The dotted arrows indicate the unmapped hydrologic connection between

these karst systems with the Garcés karst system. The codes of the tracer injection points correspond to those of Table 1. The map area corresponds to that of the "study zone" marked in Fig. 1. (B) α–β cross-section, as defined in the hydrogeological map.

3. Methods and materials

3.1. Field work

3.1.1 Instrumentation of the Garcés Cave

The Garcés Cave corresponds to the lowest zone of the Garcés System (Fig. 4). The entrance is to an old upwelling point that has been left hang. Currently, the water that overflows through Sump-1 (locally known as Silviá's sump) discharges in the Arazas river bed during the low-flows periods and through a set of trop-pleins located at different levels on the wall of the left bank of the Arazas river during the high-flows events triggered by both long rainy periods and high intensity rainfall events.

Two Diver® (Van Essen Instruments, 2016) devices were installed inside the Garcés Cave: a Baro-Diver just after the main cave entrance to register the air pressure and temperature variations in the cave and a CTD-Diver in Sump-1 to measure the variations of groundwater column and the corresponding groundwater temperature (T_{GW}) and electrical conductivity (EC_{GW}). Besides, two fluorimeters GGUN-FL24 were installed in Sump-1 to be able to measure 4 different fluorescent dye tracers at the same time. All the installed devices were programmed for measuring hourly their corresponding variables. The spring discharge is obtained as a function of the measured groundwater column through an empirical relationship.

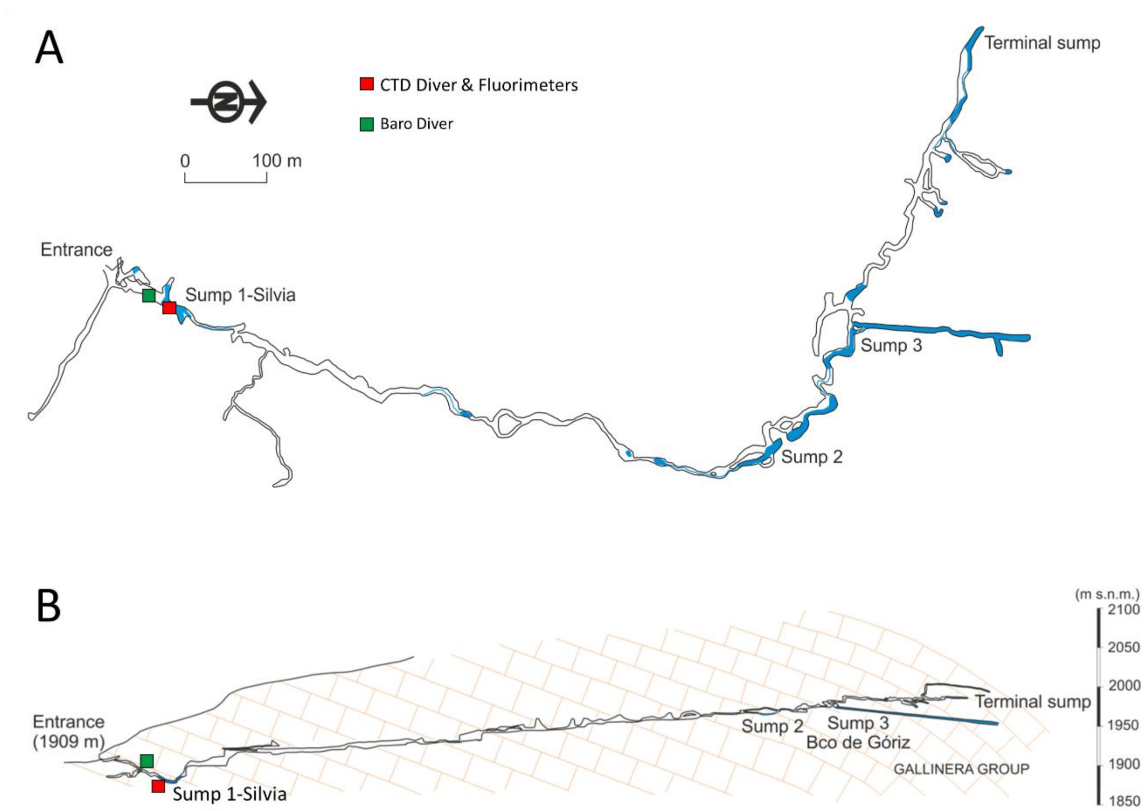

Fig. 4. Plan view (A) and cross section (B) of the Garcés karst system. The location of field instruments is also indicated.

3.1.2 Groundwater sampling

Since Jun 2018, periodical monthly GW sampling has been carried out in Sump-1 (Fig. 4). In all cases, the EC_{GW}, pH and T_{GW} were measured on site (Fig. 5). The isotope content in the water samples were determined at the Stable Isotopes Laboratory of the UAM (Universidad Autónoma de Madrid). The $\delta^{18}O$ and $\delta^{2}H$ contents were analysed by pyrolysis in a Thermo Scientific FlashEA™ 1112 HT Elemental Analyzer coupled to a DELTA V™ IRMS System. The measurement errors for $\delta^{18}O$ and $\delta^{2}H$ are ±0.1 and ±1‰, respectively. All results are given relative to the V-SMOW standard.

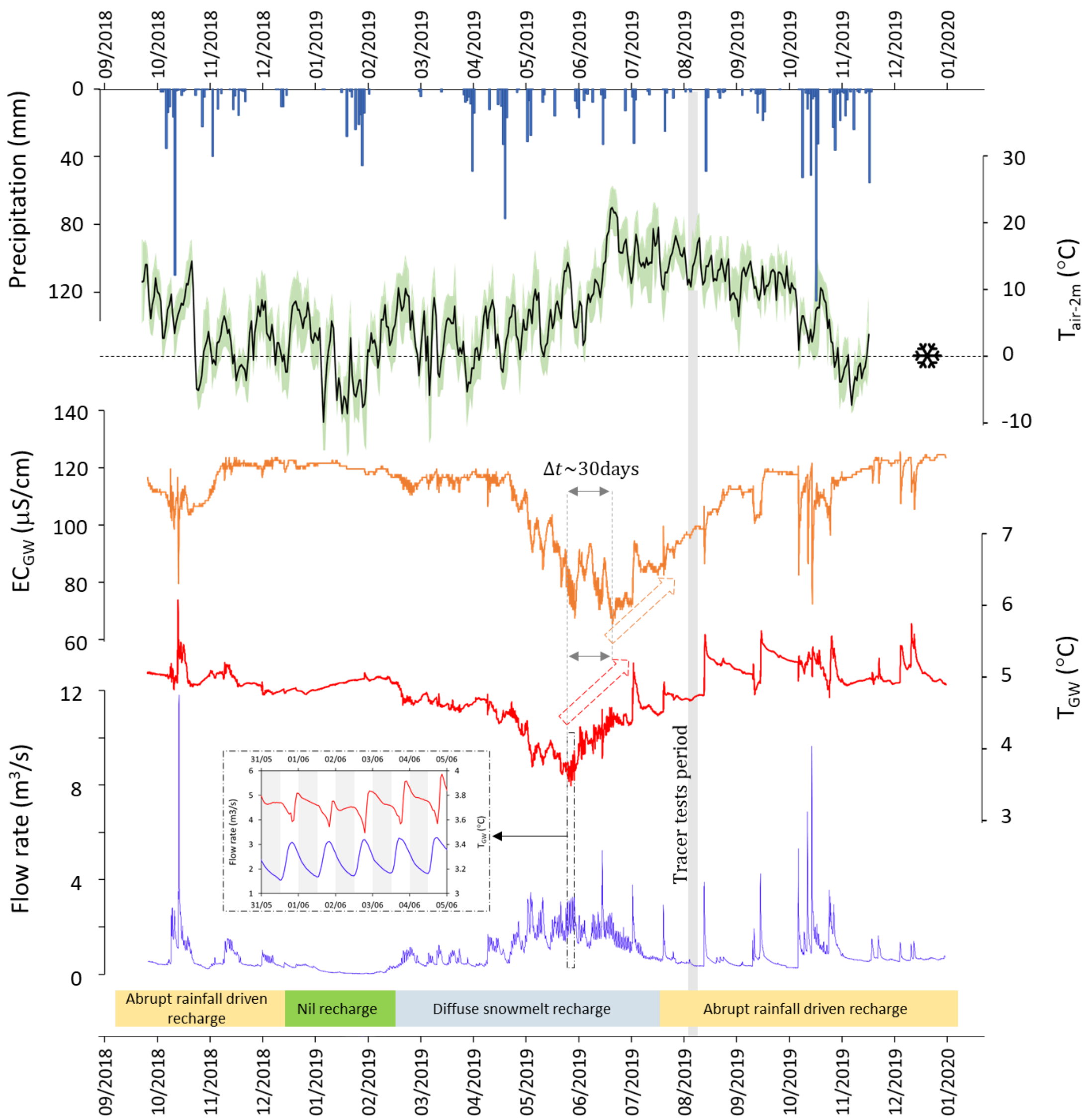

Fig. 5. From top to bottom: daily precipitation (mm); air temperature at 2 m ($T_{air\text{-}2m}$; °C) at the Góriz meteorological AEMET station, with the greenish lines indicating the maximum and minimum temperature interval (the horizontal dashed line with the snowflake symbol indicates the freezing temperature of 0 °C); electrical conductivity (EC_{GW} μS/cm) and temperature (T_{GW} °C) of groundwater in Sump-1; and Garcés Spring discharge (m^3/s) throughout the monitoring period. The inset shows the effect of the snowmelt and refreezing daily cycles on both the spring discharge and groundwater temperature for the selected time slice. The vertical grey shaded area indicates the time period in which the dye tracer tests were conducted.

3.1.3 Tracer tests

In August 2019, the members of the Otxola Espelogroup injected four fluorescent dye tracers simultaneously at different points of the Paleocene-Eocene karst system. Uranine, eosine, amino-G and naphtionate were injected into the Marboré, Cigalois, Tartracina and S60 karst systems (Fig. 3A), respectively. The distances between the tracer injection and recovery points vary between 2.8 and 4 km, and the elevation gap is between 235 and 790 m (Table 1). The time in which the dye tracer tests were conducted coincides with the low flow period of the aquifer system (Fig. 5).

Table 1: Summary of the dye tracer tests characteristics

Tracer test code	Injection point	Injected tracer	Injection point elevation[(a)] / depth[(b)]	$\Delta Z^{(c)}$	Tracer mass injected	$C_{max}^{(d)}$	Tracer test distance[(e)]
			(m a.s.l.) / (m b.g.l.)	(m)	(kg)	(ppb)	(km)
1	S-60	Naphtionate	2222 / 20	302	1.0	12.07	3.2
2	Tartracina	Amino-G	2155 / 415	235	1.5	12.88	2.8
3	Cigalois	Eosine	2710 / 0	790	0.5	1.13	3.2
4	Marboré	Uranine	2520 /120	600	0.5	0.97	4.0

(a) Meters above sea level (b) Meters below ground level; (c) Elevation gap between the tracer injection and recovery points; (d) Maximum concentration of the breakthrough curve; (e) Distances along the transects, shown in Fig. 3

3.2 Estimation of groundwater transit time and recharge elevation

3.2.1 Seasonal varying isotopic content input function

The isotopic content of GW (groundwater) in Sump-1 shows a seasonal dependence that can be described by a sinusoidal function $\delta_{\mathrm{GW}}(t)$, with $\bar{\delta}_{\mathrm{GW}}$ and $A_{\delta_{\mathrm{GW}}}$ the corresponding mean value $\bar{\delta}$ and amplitude A_{δ}, respectively (Fig. 6).

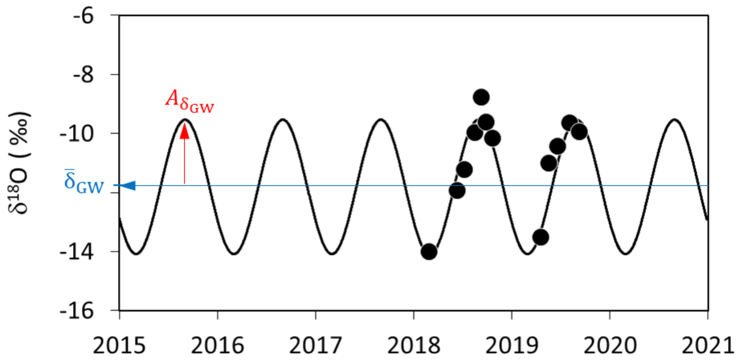

Fig. 6. Observed (circles) and EPM fitted (line) $\delta^{18}O$ content in groundwater in Sump-1. $\bar{\delta}_{GW}$ and $A_{\delta_{GW}}$ are the sinusoidal mean value and amplitude, respectively.

The seasonal behaviour observed in $\delta_{GW}(t)$ is the consequence of both a small aquifer transit time and the seasonal dependence of the isotopic content of precipitation $\delta_P(t)$. The seasonal variation in $\delta_P(t)$ shows lighter and heavier isotopic compositions in summer and winter, respectively, which agrees with the well-established relationship between isotopic fractionation and temperature (Clark and Fritz, 1997). As it happens to GW, $\delta_P(t)$ can be also described by a sinusoidal function with the corresponding $\bar{\delta}_P$ and A_{δ_P}. Aside, $\bar{\delta}_P$ and A_{δ_P} depend on elevation. This can be approached by a linear relationship between these two variables and elevation. $\bar{\delta}_P(Z)$ and $A_{\delta_P}(Z)$ are known as the “Isotopic Altitudinal Line” (IAL) and the “Amplitude Altitudinal Line” (AAL), respectively, and have to be determined empirically on site (Poage and Chamberlain, 2001; Jódar et al., 2016a,b; Herms et al., 2019).

The seasonal variation of the isotopic contents, $\delta_P(t)$ and $\delta_{GW}(t)$, allows estimating a mean response time of the aquifer (τ) by solving the convolution integral (Eq. 1) in the framework of lumped flow models (Małoszewski and Zuber, 1982). Eq. 1 describes the aquifer discharge $\delta_{GW}(t)$ in terms of both $\delta_P(t)$ and a system response function $g(t)$.

$$\delta_{\mathrm{GW}}(t) = \int_0^{\infty} \delta_{\mathrm{P}}(t - t')g(t')\, dt' \tag{1}$$

This solution is for invariable geometry. In the case of hydraulic changes the system is represented by the drainage/refilling porosity (often called effective porosity), which may be different, depending on capillary hysteresis in the unsaturated zone, and often much less than total porosity. The transfer of a conservative tracer depends on total porosity or on total matrix and fracture porosity in the case of dual porosity media. In this transfer case, the response time is the average transit /renovation time, which results from a transit time distribution in the flow and transport system.

In some cases, $g(t)$ can be expressed as an algebraic expression of a few parameters that include τ, the first moment of the transit time distribution (Małoszewski and Zuber, 1982; Amin and Campana, 1996). Jódar et al. (2016b) demonstrated that the Exponential-Piston model (EPM) was a good enough transit time distribution to describe the behaviour of the PNOMP aquifer. This model is actually the sequential combination of two different lumped models: (1) The Piston Flow Model (PFM) and (2) the Exponential Model (EM). The first model represents an aquifer system through which the tracer migrates with a constant velocity in the profile (i.e. piston flow), whereas the latter model considers an aquifer system with an exponential distribution of transit times. As a result, EPM describes an aquifer system consisting of two parts in line, regardless of their particular sequence, one with volume V_{PFM} and piston flow transit time distribution, and another part with volume V_{EM} with exponential distribution of transit times. The analytical expression describing the EPM system response function is provided by Eq. 2

$$g(t) = \begin{cases} 0 & t < \tau\left(1 - \frac{1}{\eta}\right) \equiv t_\tau \\ \frac{1}{\tau}\eta e^{-\frac{\eta}{\tau}t+\eta-1} & t \geq t_\tau \end{cases} \tag{2}$$

where η is the fraction of the total volume with the exponential distribution of transit times. In other words, $\eta = (V_{EM}+V_{PFM})/V_{EM}$. For $\eta = 1$, EPM equals to EM. For $\eta \to \infty$, EPM reduces to PFM.

In the case of EPM, there is an analytical solution to the convolution integral, given by (Jódar et al., 2014)

$$\delta_{GW}(t) = \frac{A_{\delta_P}(Z_R) \cdot \kappa^2}{\kappa^2 + \omega^2} \cdot \left(sin\big(\omega\big(t - (t_0 + t_\tau)\big) + \varphi\big) - \frac{\omega}{\kappa} cos\big(\omega\big(t - (t_0 + t_\tau)\big) + \varphi\big)\right) + \bar{\delta}_{GW} \tag{3}$$

where $\kappa=\eta/\tau$ and $A_{\delta_P}(Z_R)$ is the amplitude of the seasonal variation of the isotopic content of precipitation evaluated at the recharge zone elevation Z_R.

To estimate $A_{\delta_P}(Z_R)$, the method proposed by Jódar et al. (2016b) is applied. It can be summarized in a three steps approach:

1. Estimation of $\bar{\delta}_{GW}$. This is done by fitting a sinusoidal function to the observed values of the isotopic content in groundwater at the sampling point (Fig. 6).
2. Estimation of Z_R. This is done by evaluating the IAL (isotopic altitudinal line) function and comparing with the previously obtained $\bar{\delta}_{GW}$ value.
3. Estimation of $A_{\delta_P}(Z_R)$ by evaluating the AAL (amplitude altitudinal line) function for Z_R (Fig. 6). Both the IAL (Eq.4) and AAL (Eq.5) functions have been characterized by Jódar et al (2016b) for the PNOMP.

$$Z_R = -458.28 \cdot \overline{\delta^{18}\mathrm{O}}_{\mathrm{GW}} - 2981.60 \quad (4)$$

$$A_{\delta_{\mathrm{P}}} = 0.0009 \cdot Z_R + 3.08 \quad (5)$$

3.2.2 Pulse tracer input function

All the tracer tests conducted in the Paleocene-Eocene karst system of the PNOMP consisted of a direct pulse tracer injection in an active phreatic tube. This type of instantaneous tracer injection, with initial concentration C_0, is mathematically represented by a Dirac delta δ function (Eq. 6). The convolution integral (Eq. 1, where $\delta_{\mathrm{GW}}(t)$ and $\delta_{\mathrm{P}}(t)$ are replaced, without loss of validity, by $\mathrm{C_{out}}(t)$ and $\mathrm{C_{in}}(t)$, respectively) is solved to simulate the tracer breakthrough at the outlet of the system. In this case, the dispersion flow model (DM) (Małoszewski and Zuber, 1982) is used as the system response function, whose analytical expression is given by Eq. 7,

$$C_{in}(t) = C_0\delta(t) \quad \forall t \quad (6)$$

$$g(t) = \Gamma \cdot t^{-3/2} e^{-\left(\frac{1}{4P_D}\left(\frac{\tau}{t}+\frac{t}{\tau}\right)\right)} \qquad t \geq 0 \quad (7)$$

where Γ is defined by mathematical convenience as:

$$\Gamma = \sqrt{\frac{\tau}{4\pi P_D}}\; e^{\left(\frac{1}{2P_D}\right)} \quad (8)$$

P_D is the inverse of the Péclet number (Pe). Pe is a dimensionless number defined as the ratio between the advective and the diffusion/dispersion characteristic times. If Pe >1, then the advective flux is the most important transport mechanism, and conversely.

As in the case of EPM, the analytical solution to the convolution integral for DM does exist (Jódar et al., 2014) and is given by

$$C_{out}(t) = C_0 \cdot \Gamma \cdot t^{-3/2} e^{-\left(\frac{1}{4P_D}\left(\frac{\tau}{t}+\frac{t}{\tau}\right)\right)} \qquad t \geq 0 \tag{9}$$

3.3 Time series analysis

The statistical methods used in this work are the autocorrelation and the cross-correlation functions. Both methods are presented and commented briefly, followed by the hydrogeological interpretation.

The autocorrelation function r_X provides a normalized measure of the temporal dependence of the successive terms. In this work, there is a daily basis for the time series *X*(t) (Lambrakis et al. 2000). It is defined as

$$r_X(k) = \frac{C_X(k)}{C_X(0)} \tag{10}$$

$$C_X(k) = \frac{1}{N}\sum_{j=1}^{N-k}\left(X_j - \bar{X}\right)\left(X_{j+k} - \bar{X}\right) \tag{11}$$

where *N*, X_j and $\bar{X}$ are respectively the length, the *j*th term and the average value of the time series *X*(t), and *k* is the time lag.

The correlogram $C_X(k)$ allows estimating the memory capacity of the system (Mangin, 1984; Pulido-Bosch et al., 1995). The memory capacity is defined as the time lag required by the system to forget the initial time series values. From a pragmatic perspective, this happens when $r_X(k)$ is below a certain correlation threshold value comprised between 0.1 and 0.2 (Benavente et al., 1985). The slope of the correlogram function provides information of both, the karstification degree of the hydrogeological system and the groundwater reserves in the aquifer (Mangin, 1984; Padilla and Pulido-Bosch, 1995). This can be analysed from two extreme situations:

- Steep correlogram slope with short decorrelation time lag, which is associated to well-developed karst network aquifers with a fast response and therefore a low memory effect.
- Slightly decreasing correlogram slope with autocorrelation values above the correlation threshold value over a long time lag. This situation corresponds to poorly developed-activated karst network aquifers, with a large water storage and hence a large behavioural inertia or strong memory response.

Despite the easy rule of thumb, the shape of r_X may depend on factors external to the karst systems, such as the characteristics of the precipitation event (i.e. duration, distribution along the year, frequency and intensity) (Grasso and Jeannin 1994; Eisenlohr et al. 1997). As a good practise, the correlogram interpretation should be supported by additional information.

The cross-correlation function r_{XY}, provided that it exists, shows the not always evident relationship between a system input X(t) and output Y(t) signal time series, of not necessarily the same variable, such as precipitation and the electrical conductivity of the spring flow. This function is formally defined as

$$r_{XY}(k) = \frac{C_{XY}(k)}{\sigma_X \sigma_Y} \tag{12}$$

$$C_{XY}(k) = \frac{1}{N} \sum_{j=1}^{N-k} \left(X_j - \bar{X}\right)\left(Y_{j+k} - \bar{Y}\right) \tag{13}$$

Where $C_{XY}(k)$ is the cross-correlogram function and σ_X and σ_{Y} are the standard deviations of the time series X(t) and Y(t), respectively. If the input signal X(t) into the aquifer system corresponds to a random variable, then the cross-correlation function provides the system response function. As can be shown from equation 13, $r_{XY}(k)$ is not symmetrical if the time series are swapped (i.e. $r_{XY}(k) \neq r_{YX}(k)$).

The shape of $r_{XY}(k)$ helps to identify causal relationships between the input and the output system functions (Larocque et al., 1998). Following this line, if $r_{XY}(k) > 0$ and $k > 0$, then the system input X(t) affects the system output function Y(t). The opposite happens when $r_{XY}(k) > 0$ but $k < 0$. Additionally, when $r_{XY}(k)$ is symmetrical respect the lag origin (k = 0), then the input signal does not influence the output one. In this case, the evolution of both signals is synchronously driven by a third independent signal to be identified by means of a more detailed analysis.

The r_{XY} function provides the time delay between the input and output functions at places of maximum similarity. This delay gives an idea of the functional karstification degree of the aquifer. Moreover, the length of such delay provides an estimation of both the pressure pulse transfer times and the advective transit time of a particle migrating through the aquifer (Panagopoulos and Lambrakis, 2006). Therefore, as in the previous case, the shape of $r_{XY}(k)$ allows classifying the karst aquifer as something in between two extreme cases (Mangin, 1984; Padilla and Pulido-Bosch, 1995):

- Steep cross-correlation slope without or with a small delay of several days are associated to well-developed karst systems, whose well organized channel network favors both a short response time and a fast aquifer drainage.

- A gentle slope with a long time delay of several weeks, which is associated to poorly drained karst aquifers with long response times, even greater than several months, and large water storage.

4. Results and Discussion

The measured hydrograph (Fig. 5) reveals that base flow and quick flow coexist in the karst system discharge. Nevertheless, during winter and early spring, base flow clearly dominates while quick flow is almost absent. At a first glance, this behaviour would suggest the existence of a deficiently organized system and a poorly developed karst conduits network.

The results of the autocorrelation analysis show a very small memory effect of 2 days for P, whose autocorrelation function resembles a white noise signal (Fig. 7A). The autocorrelation of Q_{GW} decreases fast and presents an initial first stage with a steep slope during 10 days, which is associated to discharge through the karst conduits. After that time, the slope decreases to the point in which the autocorrelation signal becomes statistically not significant 50 days later. The two slopes in the autocorrelation function of Q_{GW} reveal that the aquifer is a binary karst system, with a total memory effect of 1.5 months for $Q_{GW,}$ which is enough to give to the system some storage that allows water resources regulation capacity.

The fast reaction of the karst conduit driven discharge can be observed in the cross-correlation function between P and Q_{GW} (Fig. 7B), giving $r_{XY}(0)$ = 0.35, where the reaction of the Garcés Spring discharge to precipitation becomes statistically negligible after 2 days (r_{XY} = 0.15). Aside, the maximum cross-correlation between Q_{GW}-P is lower than that for the other explored cases which consider Q_{GW} (i.e. Q_{GW}-T_{GW}, Q_{GW}-EC_{GW}), indicating that rainfall does not influence greatly the flowrate discharge of the Garcés Spring in the mid- to long-term. Moreover, the shape of this cross-correlation function shows some symmetry with respect to the lag origin, pointing out the existence of other mechanisms behind the scene, such as snowmelt, which drive Q_{GW}. In fact, there is a negative correlation r_{XY} between Q_{GW} and both T_{GW} and EC_{GW}. This points to the effect of cold and low mineralized meltwater as the main source for aquifer recharge.

The dissymmetry, the high values of $r_{XY}(k)$ and the similar slopes for positive k values in the other cross-correlation functions underlines the interdependence between EC_{GW}, T_{GW} and Q_{GW}, which is related with the percolation of in-transit recharge through the unsaturated zone, where the infiltrated water is mineralized and gets warmer along the percolating flow lines. This is supported by the positive r_{XY} of the pair T_{GW} and EC_{GW} for $k > 0$. Moreover, the long delay between Q_{GW} as input function and both T_{GW} (~ 4 months) and EC_{GW} (~ 5-6 months) can be ascribed to the travel time of the infiltrated water pulse mostly in the unsaturated zone but also in the saturated zones (Brown, 1973).

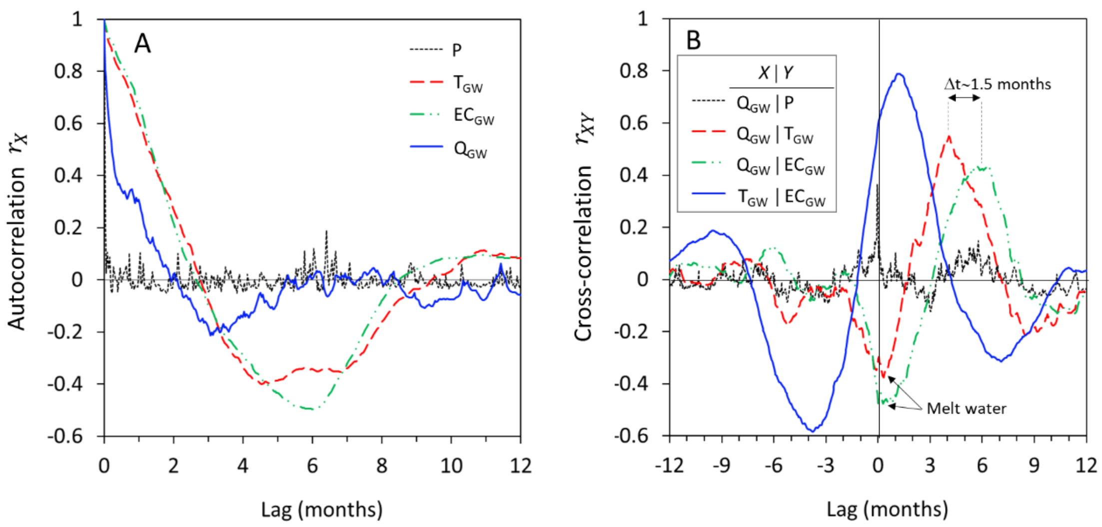

Fig. 7. Correlation dependence on lag. (A) Correlograms for precipitation (P, dotted line), and groundwater discharge (Q_{GW}, line), temperature (T_{GW}, dashed line) and electrical conductivity (EC_{GW}, dashed-dotted line). (B) Cross-correlograms for Q_{GW} and P (dotted line), Q_{GW} and T_{GW} (dashed line), Q_{GW} and EC_{GW} (line), and T_{GW} and EC_{GW} (dashed-dotted line).

The short delay in the cross-correlation Q_{GW}-P reflects the hydraulic effect between precipitation, fast recharge through the conduit system and spring discharge, whereas the other cross-correlation functions (i.e. Q_{GW}-T_{GW}, Q_{GW}-EC_{GW}) show a longer delay, reflecting the effect of an environmental tracer transport effect through the aquifer connected porosity structure. Moreover, cross-correlation Q_{GW}-EC_{GW} is delayed 1.5 months respect to Q_{GW}-T_{GW}, indicating that groundwater temperature in the connected porosity zone equilibrates sooner with the respective aquifer conditions, while EC_{GW} tend to be conserved but for some exchange with slow renovation water in the saturated and in the saturated zone. The currently documented existence of mostly temporal perched aquifers is what explains the response time difference between discharge and transport.

The Garcés cave system is the terminal drainage of the karst structure developed in the Paleocene-Eocene limestones of the PNOMP in the Ordesa valley sector. For the monitoring period, the discharge of the Garcés Spring shows a seasonal behaviour which is driven by the origin of recharge (Fig. 5). On the one hand, the precipitation (P) events of late spring, summer and autumn generate a sudden response in terms of the spring discharge (Q_{GW}), T_{GW} and EC_{GW}. During these periods, the temperature of the meteoric water that recharges the aquifer is higher than T_{GW}. Besides, the EC associated to precipitation (i.e. rainfall and snowmelt) infiltrating into the system, typically presents a low value around 20 μS/cm (Lambán et al., 2015), which is always lower than EC_{GW}, due to physicochemical, chemical and isotopic processes during recharge. Therefore, T_{GW} and EC_{GW} show pulses in response to rainfall events, of increase in summer and of decrease in autumn. The synchronicity between the rainfall event and the fast response of $Q_{GW,}$ T_{GW} and EC_{GW} is due to the quick rainfall infiltration through the most conductive karst features, including swallow holes and wide fractures (supplementary materials).

On the other hand, in late autumn, winter and spring precipitation fall as snow. As a result, the inflows to the system are mostly controlled by snowmelt. From January to March 2019, the discharge of the Garcés Spring shows a long recession curve that indicates the nil contribution of precipitation to recharge. During this period, EC_{GW} remains stable and T_{GW} shows a slight increasing trend, reflecting the physicochemical fingerprint of the in-transit recharge (Q_{iTR}). This corresponds to the contribution of water percolating slowly through the hydrologically connected porosity of the vadose zone, including small fractures and joints, to the total recharge. From March to June 2019 the day time gets longer, the sun elevation becomes higher and the air temperature rises accordingly. As a result, the snowmelt process is activated until the snow pack on the soil surface vanishes. During this period, the cold snowmelt recharges the aquifer system through all the hydrologic features existing in the ground, regardless of their entity (sinkholes, grikes, joints, etc.). This recharge is reflected in the increasing trend of Q_{GW}, with some soft peaks, and the decreasing trend of both T_{GW} and EC_{GW}. Besides the Q_{GW} and T_{GW} trends of this period, these variables also show daily fluctuations that reflect the cycle of (1) morning snowmelt with the corresponding cold water fast infiltration through the most conductive features, and almost downward gravity driven flow through shafts and canyons, which generates both an increase in Q_{GW} and a decrease in T_{GW}, and (2) the evening refreezing that cuts the cold recharge inflows from snowmelt into the system. This allows T_{GW} and Q_{GW} to recover the corresponding values of the system inflows from the in-transit recharge. There is a time lag of 10 h for the melt-water pulse to get Sump-1. This short lag underlines the high velocity of groundwater flowing through the conduits and therefore their corresponding short transit times. This is closely related with the hydraulic effect highlighted by the Q_{GW}-P cross-correlation function.

The mean isotopic content ($\delta^{18}O$) in the Garces Spring groundwater discharge is -11.81 ‰. The associated recharge zone elevation (z_R, Eq. 4) is 2429 m. a.s.l.. This value is consistent with those obtained by Jódar et al (2016b) for other springs in the PNOMP. At elevations above 2400 m a.s.l. the snow covers the ground surface during long periods of the year. Nevertheless, the summer high temperatures reduce the presence of snow to the highest elevation zones of the PNOMP. Consequently, from June 2019 onwards Q_{GW} decreases and T_{GW} increases. Nevertheless, the evolution of EC_{GW}, which has been similar to T_{GW} up to this moment, shows 1.5 month delay respect to the observed increasing trend in $T_{GW.}$ This is the consequence of the gradual extinction of the snowmelt inflows into the system, while Sump-1 still receives the contribution of the in-transit recharge through the unsaturated zone. This one and a half month delay between EC_{GW} and T_{GW} is clearly reflected in the corresponding cross-correlogram (Fig. 7B).

It is possible to estimate the contribution of in-transit recharge to the total inflows to Sump-1 using EC as an environmental tracer and conducting a water mass balance given by,

$$Q_{GW} = Q_{FR} + Q_{iTR} \qquad (14)$$

$$EC_{GW}Q_{GW} = EC_{FR}Q_{FR} + EC_{iTR}Q_{iTR} \tag{15}$$

where Q_{GW} is the groundwater discharge in the Garcés Spring and EC_{GW} is the corresponding EC which is continuously measured by the CTD-Diver in Sump-1 (Fig. 5). Q_{FR} is the fast recharge entering the system though the conduits and EC_{FR} is the corresponding EC, whose value is approximated by the 20.55 μS/cm mean EC value of precipitation in the PNOMP (Lambán et al., 2015). Q_{iTR} is the in-transit recharge contribution to the total karst system inflows and EC_{FR} is the corresponding EC value, which is estimated as the maximum EC value observed in GW throughout the monitoring period (125 μS/cm). The solution of the equation system in terms of Q_{iTR} and Q_{FR} is provided by

$$Q_{iTR} = \left(\frac{EC_{GW} - EC_{FR}}{EC_{iTR} - EC_{FR}}\right) \cdot Q_{GW} \tag{16}$$

$$Q_{FR} = Q_{GW} - Q_{iTR} \tag{17}$$

For the hydrological year 2018-2019, the estimated mean values of Q_{iTR} and Q_{FR} are 0.61 m^3/s and 0.20 m^3/s, respectively. As the mean system discharges Q_{GW} is 0.81 m^3/s, the contributions of Q_{iTR} and Q_{FR} to Q_{GW} are 74.9 % and 25.1%, respectively. This result highlights the main role of connected porosity and small joints and fractures as water resource storage in the Paleocene-Eocene karst system, and the importance of the in-transit recharge to release 3/4 of the total discharge to the downstream depending ecosystems. Perrin et al. (2003) found similar results for the Milandre karst system in the Swiss folded and overthrusted Jura Mountains. Nevertheless, in this case, not only the epikarst played a major role as water resources storage, as the existence of a thick soil horizon provided additional water storage, while protecting the aquifer from external contaminants that may enter the system. In this line, it is important to note the lack of a well-developed soil layer on top the epikarst zone in the PNOMP. This layer would enhance both the water storage capacity and the protection of the groundwater system in front of a contaminant spill event.

The water storage capacity of the hydrologic system is not the only key factor. The transit time is another relevant subject of the aquifer that informs about how long takes the in-transit recharge to get into the system outflow site (τ_{iTR}). This information is obtained through the calibration of the EPM model parameters (τ and η; Eq. 3) to fit the observed variation of the isotopic content of GW (Fig. 6). The obtained values of η and τ_{iTR} are 3.87 and 1.3 yr (475 days), respectively. The η value points out that V_{PFM} is $2.87 \cdot V_{EM}$, thus accentuating the contribution of the vadose zone to the transit time distribution for the whole hydrological system (see section 3.2.1). The small τ_{iTR} value stresses the vulnerability of the whole hydrogeological system to the impact of climate change and the associated warming trend, which will generate a decrease in the snow precipitation events, thus modifying the recharge system function in terms of a decrease in the snowmelt infiltration, as that obtained by Chen et al., (2018) for a high elevation karst aquifer system in the northern Alps at the end of the 21st century. Moreover, in keeping with those given expectations, Pardo- Igúzquiza et al., (2019) obtained for the same future horizon a recharge decrease of 53% in the aquifer system of Sierra de las Nieves, a privileged observatory of the early impact of climate change in continental Europe, since it is the southernmost high mountain karst system of the Iberian Peninsula.

The τ_{iTR} value can be used to estimate the water volume in the connected porosity, joints and fractures (v_{iTR}) of the karst system, which is given by

$$V_{iTR} = Q_{GW} \cdot \tau_{iTR} \tag{18}$$

For the hydrological year 2018-2019, the value obtained for V_{iTR} is 24.9 hm^3. This volume represents 39% and 24% of the mean annual water consumption in the cities of Zaragoza and Barcelona, respectively (Penagos 2007; Barcelona City Council, 2018), and highlights the moderate water resources regulation capacity that has the connected porosity part of the aquifer, despite the associated short memory effect in Q_{GW} (Fig. 7A). In fact, the memory effect does not reflect correctly the regulation capacity of the system, but it is more affected by fast recharge. The correlogram does not depend on the values of the of the discharge series but rather on the form of the peaks (Grasso and Jeannin, 1984): the sharper the hydrograph the more rapid the decrease of the correlogram.

The fluorescent dye tracers were used to characterize the high conductive features of the karst system through which the fast recharge (Q_{FR}) enters the system. The tracer tests were interpreted by fitting the parameters τ and P_D of Eq. 9, which is the solution of the convolution integral (Eq. 1) for the case of considering the dispersion flow model (DM) as the system response function (Eq. 7). Table 2 shows the calibrated transit time (τ_{FR}) and the Péclet number (Pe) for each tracer test, and figure 8 shows the observed and computed concentrations for every tracer test. In each case, the concentrations are normalized by the observed maximum concentration of the test.

The tracer recovery decreases as both the distance and the elevation gap between the tracer injection point and the outlet of the system increases. This result may be the consequence of local channel diversions that feed non-controlled diffuse discharge zones in the hydrogeological basin, according to the form of the breakthrough curves (BC) for tracer tests 3 and 4 (Fig. 8C and 8D). Nevertheless, the mapped karst systems show how karst drainage is locally related to fractures and thrust faults. Therefore, some mass tracer might migrate along steep tectonic structures through the low permeability Marboré Formation materials towards the underlying Upper Cretaceous aquifer (Lambán et al., 2015). This process implies the possible existence of a deep regional drainage mechanism in the PNOMP.

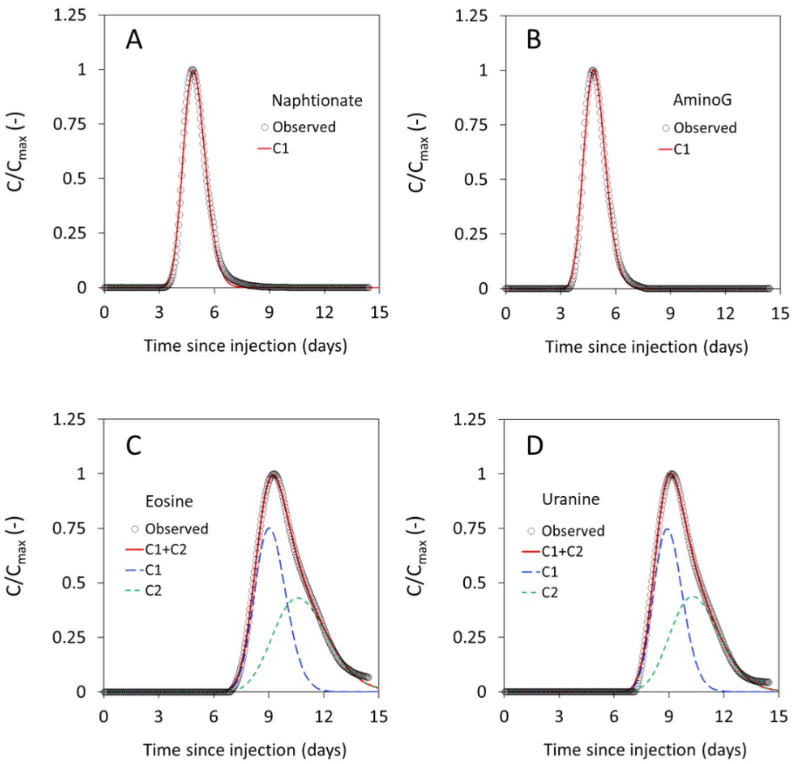

Fig. 8. Observed (circles) and calibrated (continuous and dashed lines) breakthrough curves (BC) for the tracer tests conducted in this work. (A) Tracer test 1, (B) Tracer test 2, (C) Tracer test 3, and (D) Tracer test 4. In the case of tracer test 3 and 4, a two-flow path model is used. Therefore, C1 and C2 correspond to the BC associated to each one of the flow paths, and C1+C2 corresponds to the sum of BC1 and BC2, which is the BC measured at the outflow site of the system.

The transit times are close to 5 days for tracer tests 1 and 2, and close to 9 days for tracer tests 3 and 4, in coherence with longer distance and elevation gap to travel in the case of these two latter tracer tests. In all cases, the estimated Péclet number (P*e*; Table

2) is much greater than 1, revealing advection as the main transport mechanism through the conduits of the karst system, as one would expect from the symmetrical shape of the measured BCs (Fig. 8). The minor role played by dispersion is directly related with the geometrical structure of the conduits in the karst system. According to Hauns et al., (2001) and Berglund et al., (2020), the conduits geometry, especially in the overly tortuous cases, is the dominant factor generating tracer dispersion at a spatial scale of 10^2 to10^3 m. An advective tracer transport should be likely related with simple conduits geometries. To illustrate this, the supplementary materials include some representative examples of the conduits inside the PNOMP karst system. As can be shown, they present a gentle slope and tubular cross section, without many irregularities, which are typical features of the water table cave pattern.

During the tracer tests period, the groundwater flow regime in the conduits was laminar, as indicated by the low Reynolds number (R_e; Table 2). This reflects the slow discharge of the connected porosity domain into the saturated zone, which is finally guided through the conduits towards the aquifer discharge point in the Garcés Spring.

The water storage in the high conductive features can be estimated, as a first approach, as follows (Małoszewski et al., 2002)

$$V_{FR} = Q_{FR} \cdot \tau_{FR} \tag{19}$$

Taking into account the τ_{FR} values obtained for the tracer test conducted in this work, V_{FR} ranges between 0.076 and 0.156 hm^3 (Table 2).

The ratio V_{iTR}/V_{FR} is larger than 10^3, which is consistent with the low memory effect associated to the conduits by the autocorrelation of Q_{GW}. Moreover, the ratio value underpins the important role played by the connected porosity of the vadose zone as water resources storage.

Similar results of V_{FR} and τ_{FR} were obtained by Lauber and Goldscheider (2014) for a number of tracer tests conducted in the alpine karst system of the Wetterstein Mountains during the aquifer low flow period. The short transit times indicate the existence of well-drained fractures and fissures. Despite of the similarities between the obtained results, the observed BCs in the Wetterstein Mountains karst system presented a long tail. This detail reveals that tracer explored a large karst volume before reaching the sampling (discharge) point (i.e. spring). If the injection and sampling points were connected by conduits, the corresponding BC would be much less skewed than the observed ones. In fact, unlike the PNOMP, no large cave systems are known in the Wetterstein Mountains. This result stresses the importance of speleological explorations in the karst systems, as they provide direct information of the internal geometry and actual functioning of the karts systems. They are of paramount importance for correctly defining the conceptual model of the corresponding aquifers.

Table 2: Calibrated parameters of the lumped diffusion model obtained for the different BCs measured in Sump-1.

Tracer test code	Mass recovery (%)	Mean velocity[a] (m/d)	R_e[b] (-)	V_{FR} (hm^3)	Pe (-)			τ_{FR} (d)		
					Flow Path 1	Flow Path 2	Average	Flow Path 1	Flow Path 2	Average
1	95	645	1952	0.077	133.9	--	133.9	4.96	--	4.96
2	99	571	1727	0.076	136.5	--	136.5	4.90	--	4.90
3	30	319	966	0.156	229.0	104.2	166.6	9.15	10.89	10.02
4	12	409	1236	0.152	257.9	119.1	188.5	9.00	10.56	9.78
Average	59	486	1470	0.115	189.3	111.7	156.4	7.00	10.73	7.41

(a) ratio between the tracer test distance (Table 1) and the conduit mean transit time τ_{FR}; (b) Reynolds number estimated as R_e=V·L/ν, where V is the groundwater velocity, L is the channel characteristic length estimated as 0.4 m from the geometry of the flooded conduits revealed in the pictures taken during the dye tracer injection day (supplementary materials), and ν is the kinematic water viscosity, equal to 0.13 m^2/d for a water temperature 4.8 °C (Engineering ToolBox, 2004), which corresponds with T_{GW} in the Garcés Spring the day of the tracers injection.

The Paleocene-Eocene limestones of the Gallinero Formation constitute the main aquifer of the PNOMP. The hydrodynamic behaviour of this aquifer corresponds to a binary karst system with both conduit and diffuse components. The results show that the connected porosity of the formation provides 3/4 of the total groundwater discharge in the Garcés Spring, while providing almost all the water storage of the aquifer (Fig. 9). The porosity of the limestones is not known. Nevertheless, such parameter can be estimated as a first approach as

$$\phi = \frac{\mathrm{V_{iTR}} + \mathrm{V_{FR}}}{\mathrm{V_{aq}}} \tag{20}$$

where $\mathrm{V_{aq}}$ is the aquifer formation volume. $\mathrm{V_{aq}}$ can be evaluated as the product of the 18.1 km^2 aquifer surface area and the aquifer thickness, estimated to be equal to the 250 m mean thickness of the Gallinero formation (Robador et al., 2018). Taking into account these values, a connected porosity of 0.6% is obtained, which is low but still consistent with those obtained for other mountain karst systems, such as 1.5% in the Schneealpe (Maloszewski et al., 2002) or 2% in the Swabian Alps (Sauter,1993). In the case of the karst aquifer drained by the Garcés Spring, the associated dual-porosity model, in which conduit and fracture porosity co-occur by contributing 1/4 and 3/4, respectively, to the total groundwater discharge, it can be assumed that most of the flow in the saturated zone is probably Darcian. Despite of that, the combination of the small porosity with high permeability of the most conductive features of the karst aquifer results in groundwater velocities along conduits that may have important implications for contaminant transport (Worthington, 2015). The short transit times of both conduits and connected porosity minimize the degradation and dilution of possible contaminants entering the system, e.g. faecal bacteria that would be transported to the spring within a short period of time.

Moreover, the low memory of the aquifer system revealed by the autocorrelation analysis informed about the relatively small storage capacity of conduits along with the karstification degree of the system. All these characteristics enlighten the high vulnerability of the karst aquifer system drained through the Garcés Spring.

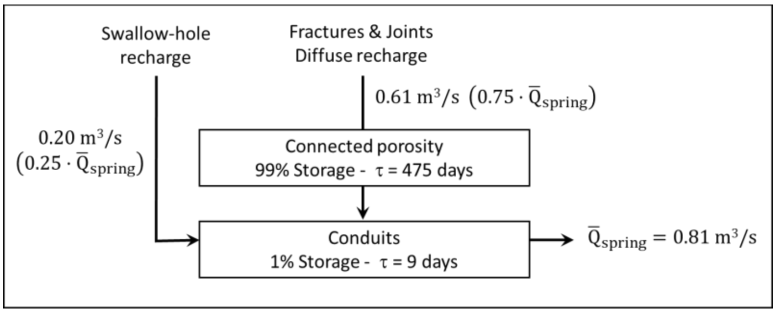

Fig. 9. Two-box model for the Paleocene-Eocene carbonate aquifer of the PNOMP, with fraction of storage (expressed in percentage of total) and residence time in each box, and groundwater flow between boxes. See text for details.

Characterizing the hydrodynamical behavior of karst systems is not easy, given the heterogeneity of the karstic massifs and the complexity of the karst networks developed inside, whose structure and complexity depends on the geological setting, the recharge rates and time (Audra and Palmer, 2011; 2015). In high mountain areas, the characterization of karst aquifers is even more difficult given the rough topography that hampers the access, transportation of materials and normal operation. Besides, the severe climatic conditions prevent accessing the area during long time periods. The karst aquifer described here has many points in common with other karst systems in high mountain zones, where diffuse infiltration of snowmelt conditions karst structure and consequently its hydrodynamic behaviour (Lauber and Goldscheider, 2014).

The snowmelt is thus the process behind the geomorphological structure and hydrodynamic behaviour of the PNOMP karst system. The mean persistence of the snow cover during 2/3 of the hydrologic year conditions the lack of both a highly developed epikarst zone and a surficial semi-confining layer. Nevertheless, the snow pack plays the same role as the surficial semi-confining layer. The snowmelt flows diffusely through the snow pack minimizing surface runoff. The slow snowmelt rate favors water infiltration through the network of joints and fractures, thus maximizing aquifer recharge while maintaining moderate drainage rates. The aquifer base flow is controlled by the in-transit recharge in the saturated zone. This flow component is Darcian and dominates the aquifer system discharge during 2/3 of the hydrologic year. The role played by the quick flow component flowing through the conduits is only relevant during late spring, summer and early autumn, which is the time when the convective storms are produced in the Pyrenees (Callado and Pascual, 2005). Taking into account that the conduits of a matured karst carry the majority of flow and control the hydrogeological behaviour of the system (e.g., White, 1988; Ford and Williams, 2007), which is not the case in the PNOMP, and the existence of an epiphreatic zone with a water table cave pattern, it seems reasonable to think that the PNOMP karst system is still young, even containing highly conductive conduits inside.

In this work, the combined use of both environmental and fluorescent dye tracers along with time series analysis of physicochemical and hydrological variables allowed to characterize the behaviour of the karst systems drained by the Garcés Spring. The applied methodology may be useful to characterize other alpine karst aquifer systems.

5. Conclusions

The snowmelt recharge controls both the geomorphological evolution and maturity of the karst system and the corresponding hydrological behaviour.

The karst system behaves as a dual-porosity aquifer, with a highly permeable domain that includes the karst conduits, and a connected porosity domain lumping joints, fractures and primary inter-particle porosity. The first one controls the system response during the rainfall events whereas the latter does it during the snow accumulation seasons until the beginning of summer with the end of thaw.

The in-transit recharge controls the T and EC dynamics in the phreatic zone. Moreover, the water storage in the system is almost linked to the connected porosity structure, which is drained at low flow rates into the saturated zone, where the groundwater flow is Darcian. Despite of that, the combination of the low porosity with the high permeability of most conductive features may have important implications for contaminant transport.

The low transit times in both the conduits and the connected porosity domains reveal the high vulnerability of the karst system to contaminant issues and the impact of climate change.

6. Acknowledgments

This research was undertaken in the framework of the PIRAGUA project. The project EFA210/16 PIRAGUA is co-founded by the European Regional Development Fund (ERDF) through the Interreg V Spain-France-Andorre Programme (POCTEFA 2014-2020) of the European Union. The authors would like to thank the Ordesa and Monte Perdido National

Park Direction (Gobierno de Aragón) and especially Elena Villagrasa from DGA, Fernando Carmena and Ignacio Gómez from SARGA, the Góriz Mountain Hut Wardens by their collaboration. Meteorological data have been provided by the Spanish Meteorological Agency (AEMET).

We are deeply grateful to OTXOLA Speleological Group (Grupo espeleología Otxola, Otxola Espeleologi taldea) for their help injecting the fluorescent dye tracers during the tracer test campaigns. Aside, we acknowledge both OTXOLA and SCC (Spéléo Club du Comminges) for providing information of the different karts systems draining the study zone.

References

AEMET/IM., 2011. Atlas Climático Ibérico–Iberian Climate Atlas. Agencia Española de Meteorología & IM. Madrid: 1–80.

Amin, I.E., and Campana, M.E., 1996. A general lumped parameter model for the interpretation of tracer data and transit time calculations in hydrologic systems. J. Hydrol. 179, 1–21. https://doi.org/10.1016/0022-1694(95)02880-3

Audra, P., and Palmer, A.N., 2011. The pattern of caves: controls of epigenic speleogenesis. Géomorphologie: relief, processus, environnement. 17(4), 359-378. https://doi.org/10.4000/geomorphologie.9571.

Audra, P., Palmer, A.N., 2015. Research frontiers in speleogenesis. Dominant processes, hydrogeological conditions and resulting cave patterns. Acta Carsologica. 44(3): 315-348. https://doi.org/10.3986/ac.v44i3.1960.

Barcelona City Council, 2018. Evolution of Water Consumption in the City of Barcelona. http://www.bcn.cat/estadistica/angles/dades/economia/consum/evoconsum/coev04.htm, Accessed date: 7 August 2018.

Benavente, J., Pulido-Bosch, A., and Mangin, A., 1985. Application of correlation and spectral procedures to the study of the discharge in a karstic system (Eastern Spain). In: Karst Water Resources, Ankara-Antalya, 67–75.

Berglund, J.L., Toran, L., Herman and E.K., 2020. Can Karst Conduit Models Be Calibrated? A Dual Approach Using Dye Tracing and Temperature. Groundwater. https://doi.org/10.1111/gwat.12988

Bögli, A., 1980. Karst Hydrology and Physical Speleology, Springer-Verlag, Berlin, 284 pp

Brown, M.C., 1973. Mass balance and spectral analysis applied to Karst hydrologie networks. Water Resources Research, 9(3), 749-752. https://doi.org/10.1029/WR009i003p00749

Callado, A., and Pascual, R., 2005. Diagnosis and modelling of a summer convective storm over Mediterranean Pyrenees. Advances in Geosciences. 2005, 2, 273-277. https://dx.doi.org/10.5194/adgeo-2-273-2005

Chen, Z., and Goldscheider, N., 2014. Modeling spatially and temporally varied hydraulic behavior of a folded karst system with dominant conduit drainage at catchment scale, Hochifen–Gottesacker, Alps. Journal of Hydrology, 514, 41-52. http://dx.doi.org/10.1016/j.jhydrol.2014.04.005

Chen, Z., Hartmann, A., Wagener, T., and Goldscheider, N., 2018. Dynamics of water fluxes and storages in an Alpine karst catchment under current and potential future climate conditions. Hydrology and Earth System Sciences, 22(7), 3807. https://doi.org/10.5194/hess-22-3807-2018

Clark, I.D., and Fritz. P., 1997. Environmental isotopes in hydrogeology. CRC Press; 1997.

Eisenlohr, L., Bouzelboudjen, M., Kiraly, L., and Rossier, Y., 1997. Numerical versus statistical modelling of natural response of a karst hydrogeological system. J Hydrol 202, 244–262. https://doi.org/10.1016/S0022-1694(97)00069-3

Engineering ToolBox, 2004. Water - Dynamic and Kinematic Viscosity. [online] Available at: https://www.engineeringtoolbox.com/water-dynamic-kinematic-viscosity-d_596.html [Accessed 23 May 2020].

Ford, D.C., and Williams, P.W., 2007. Karst Hydrogeology and Geomorphology. Wiley, Chichester, United Kingdom. 562 p.

Gabrovšek, F., and Dreybrodt, W., 2001. A model of the early evolution of karst aquifers in limestone in the dimensions of length and depth. Journal of hydrology, 240(3-4), 206-224. https://doi.org/10.1016/S0022-1694(00)00323-1

Goldscheider, N., 2005. Fold structure and underground drainage pattern in the alpine karst system Hochifen-Gottesacker. Eclogae Geologicae Helvetiae, 98(1), 1-17. https://doi.org/10.1007/s00015-005-1143-z

Goldscheider, N., Chen, Z., Auler, A.S., Bakalowicz, M., Broda, S., Drew, D., Hartmann, H., Jiang, G., Moosdorf, N., Stevanovic, Z., and Veni, G., 2020.

Global distribution of carbonate rocks and karst water resources. Hydrogeology Journal. https://doi.org/10.1007/s10040-020-02139-5

Göppert N., and Goldscheider, N., 2008. Solute and colloid transport in karst conduits under low- and high-flow conditions. Vol. 46, No. 1, 61–68. Ground Water. https://doi.org/10.1111/j.1745-6584.2007.00373.x

Grasso, D.A., and Jeannin, P.Y., 1994. Etude critique des méthodes d’analyse de la réponse globale des systèmes karstiques. Application au site de Bure (JU, Suisse): Bulletin d’Hydrogéologie Neuchâtel, 13, 87-113.

Gremaud, V., Goldscheider, N., Savoy, L., Favre, G., and Masson, H., 2009. Geological structure, recharge processes and underground drainage of a glacierised karst aquifer system, Tsanfleuron-Sanetsch, Swiss Alps. Hydrogeology journal, 17(8), 1833-1848. https://doi.org/10.1007/s10040-009-0485-4

Hauns, M., Jeannin, P.Y., and Atteia, O., 2001. Dispersion, retardation and scale effect in tracer breakthrough curves in karst conduits. Journal of hydrology, 241(3-4), 177-193. https://doi.org/10.1016/S0022-1694(00)00366-8, 2001

Häuselmann, P., 2019. Solution caves in regions of high-relief. In Encyclopedia of Caves (pp. 943-954). Academic Press.

Herms. I., Jódar, J., Soler, A., Vadillo, I, Lambán, L.J., Martos-Rosillo, S., Núñez, J.A., Arnó, G., and Jorge, J., 2018. Contribution of isotopic research techniques to characterize high-mountain-Mediterranean karst aquifers: The Port del Comte (Eastern Pyrenees) aquifer. Science of the Total Environment, https://doi.org/10.1016/j.scitotenv.2018.11.188

Jódar, J., Lambán. L.J., Medina, A., and Custodio, E., 2014. Exact analytical solution of the convolution integral for classical hydrogeological lumped-parameter models and typical input tracer functions in natural gradient systems. J. Hydrol., 519: 3275–3289. https://doi.org/10.1016/j.jhydrol.2014.10.027

Jódar, J., Custodio, E., Liotta, M., Lambán, L.J., Herrera, C., Martos-Rosillo, S., Sapriza, G., and Rigo, T., 2016(a). Correlation of the seasonal isotopic amplitude of precipitation with annual evaporation and altitude in alpine regions. Sci. Total Environ., 550, 27-37. https://doi.org/10.1016/j.scitotenv.2015.12.034

Jódar, J., Custodio, E., Lambán, J.L., Martos-Rosillo, S., Herrera, C., and Sapriza, G., 2016(b): Vertical variation in the amplitude of the seasonal isotopic content of rainfall as a tool to jointly estimate the groundwater recharge zone and transit times in the Ordesa and Monte Perdido National Park aquifer system, north-eastern Spain. Science of The Total Environment, https://doi.org/10.1016/j.scitotenv.2016.08.117

Jouves, J., Viseur, S., Arfib, B., Baudement, C., Camus, H., Collon, P., and Guglielmi, Y., 2017. Speleogenesis, geometry, and topology of caves: A quantitative study of 3D karst conduits. Geomorphology. 298, 86-106. https://doi.org/10.1016/j.geomorph.2017.09.019.

Kaufmann, G., 2002. Karst aquifer evolution in a changing water table environment. Water Resources Research, 38(6), 26-1. https://doi.org/10.1029/2001WR000256

Lambán, L.J., Jódar, J., Custodio, E., Soler, A., Sapriza, G., and Soto, R., 2015. Isotopic and hydrogeochemical characterization of high-altitude karst aquifers in complex geological settings. The Ordesa and Monte Perdido National Park (Northern

Spain) case study. Sci. Total Environ., 506, 466-479. https://doi.org/10.1016/j.scitotenv.2014.11.030

Lambrakis, N., Andreou, A.S., Polydoropoulos, P., Georgopoulos, E., and Bountis, T., 2000. Non-linear analysis and forecasting of a brackish karstic spring. Water Resour. Res. 36 (4), 875–884. https://doi.org/10.1029/1999WR900353

Larocque, M., Mangin, A., Razack, M., and Banton, O., 1998. Contribution of correlation and spectral analyses to the regional study of a large karst aquifer (Charente, France). Journal of hydrology, 205(3-4), 217-231. https://doi.org/10.1016/S0022-1694(97)00155-8

Lauber, U., and Goldscheider, N., 2014. Use of artificial and natural tracers to assess groundwater transit-time distribution and flow systems in a high-alpine karst system (Wetterstein Mountains, Germany). Hydrogeology journal, 22(8), 1807-1824. https://doi.org/10.1007/s10040-014-1173-6

Małoszewski, P., and Zuber, A., 1982. Determining the turnover time of groundwater systems with the aid of environmental tracers, I. Models and their applicability. J. Hydrol. 57, 207–231. https://doi.org/10.1016/0022-1694(82)90147-0

Małoszewski, P., Stichler, W., Zuber, A., and Rank, D., 2002. Identifying the flow systems in a karstic-fissured-porous aquifer, the Schneealpe, Austria, by modelling of environmental ^{18}O and ^{3}H isotopes. Journal of Hydrology 256, 48–59. https://doi.org/10.1016/S0022-1694(01)00526-1

Mangin, A., 1984. Pour une meilleure connaissance des systèmes hydrologiques à partir des analyses corrélatoire et spectrale. Journal of hydrology, 67(1-4), 25-43. https://doi.org/10.1016/0022-1694(84)90230-0

Meeks, J., and Hunkeler, D., 2015. Snowmelt infiltration and storage within a karstic environment, Vers Chez le Brandt, Switzerland. Journal of Hydrology, 529, 11-21. https://doi.org/10.1016/j.jhydrol.2015.06.040

Ortega-Becerril, J.A., Polo, I., and Belmonte, A., 2019. Waterfalls as Geological Value for Geotourism: the Case of Ordesa and Monte Perdido National Park. Geoheritage, 11(3), 1199-1219. https://doi.org/10.1007/s12371-019-00366-1

Padilla, A., and Pulido-Bosch, A., 1995. Study of hydrographs of karstic aquifers by means of correlation and cross-spectral analysis. J. Hydrol. 168, 73–89. https://doi.org/10.1016/0022-1694(94)02648-U

Panagopoulos, G., and Lambrakis, N., 2006. The contribution of time series analysis to the study of the hydrodynamic characteristics of the karst systems: Application on two typical karst aquifers of Greece (Trifilia, Almyros Crete). Journal of Hydrology, 329(3-4), 368-376. https://doi.org/10.1016/j.jhydrol.2006.02.023

Pardo-Igúzquiza, E., Collados-Lara, A.J., and Pulido-Velazquez, D., 2019. Potential future impact of climate change on recharge in the Sierra de las Nieves (southern Spain) high-relief karst aquifer using regional climate models and statistical corrections. Environmental Earth Sciences, 78(20), 598. https://doi.org/10.1007/s12665-019-8594-4

Penagos, G., 2007. Systems Analysis of Zaragoza Urban Water System (Spain): A Preliminary Assessment of Environmental Sustainability. MSc Thesis ES 07.27. UNESCO-IHE Institute for Water Education, Delft, the Netherlands.

Perrin, J., Jeannin, P.Y., and Zwahlen, F., 2003. Epikarst storage in a karst aquifer: a conceptual model based on isotopic data, Milandre test site, Switzerland. Journal of hydrology, 279(1-4), 106-124. https://doi.org/10.1016/S0022-1694(03)00171-9

Poage, M.A., and Chamberlain, C.P., 2001. Empirical relationships between elevation and the stable isotope composition of precipitation and surface waters: considerations for studies of paleoelevation change. Am. J. Science 301 (1), 1–15. http://dx.doi.org/10.2475/ajs.301.1.1

Pulido-Bosch, A., Padilla, A., Dimitrov, D., and Machkova, M., 1995. The discharge variability of some karst springs in Bulgaria studied by time series analysis. Hydrol. Sci. J. 40 (4), 517–532. https://doi.org/10.1080/02626669509491436

Robador A., Belmonte A., Carcavilla L., Samsó J.M., and Martínez-Rius A., 2018. Mapa Geológico del Parque Nacional de Ordesa y Monte Perdido a escala 1:25.000. Seri GeoNatur. Edited by IGME.

Rossi, C, Muñoz, A, and Cortel A, 1997. Cave development along the water table in the Cobre System (Sierra de Peñalabra, Cantabrian Mountains, Spain, Proceedings of the 12th International Congress of Speleology, 1, 179–185

Sauter, M., 1993. Double porosity models in karstified limestone aquifers: Field validation and data provision, in Günay, G., Johnson, A.I., and Back, W., eds., Hydrogeological Processes in Karst Terranes: International Association of Hydrological Sciences Publication 207, 261–279.

Séguret, M., 1972. Etude tectonique des nappes de series décollées de la partie centrale du versant sud des Pyrénées. Caractère synsédimentaire, rôle de la compression et de la gravité. Thèse Doct. Publ. USTELA. Série Géol. Montpellier. 155 p

Smart, C.C., 1996. Statistical evaluation of glacier boreholes as indicators of basal drainage systems. Hydrological Processes, 10(4), 599-613. https://doi.org/10.1002/(SICI)1099-1085(199604)10:4<599::AID-HYP394>3.0.CO;2-8

Stevanovic, Z., 2019. Karst waters in potable water supply: a global scale overview. Environ Earth Sci 78(23), 662. https://doi.org/10.1007/s12665-019-8670-9

Van Essen Instruments, 2016. Product Manual Diver (Last access 22/04/2020) https://www.eijkelkamp.com/download.php?file=M21111e_Diver_118b.pdf

Viviroli, D., Dürr, H.H., Messerli, B., Meybeck, M., and Weingartner, R., 2007. Mountains of the world— water towers for humanity: typology, mapping and global significance. Water Resources Research 43 (7), W07447. https://doi.org/10.1029/2006WR005653

White, W.B., 1988. Geomorphology and Hydrology of Karst Terrains. Oxford University Press, New York. 464 p.

Worthington, S.R., 2015. Characteristics of channel networks in unconfined carbonate aquifers. Geological Society of America Bulletin, 127(5-6), 759-769. https://doi.org/10.1130/B31098.1

Zeng, C., Liu, Z., Yang, J., and Yang, R. 2015. A groundwater conceptual model and karst-related carbon sink for a glacierized alpine karst aquifer, Southwestern China. Journal of Hydrology, 529, 120–133. https://doi.org/10.1016/j.jhydrol.2015.07.027

Supplementary material for on-line publication only

Click here to download Supplementary material for on-line publication only: SupplementaryMaterial.docx

***conflict of Interest Statement**

Declaration of interests

☒ The authors declare that they have no known competing financial interests or personal relationships that could have appeared to influence the work reported in this paper.

☐The authors declare the following financial interests/personal relationships which may be considered as potential competing interests:

The authors: The authors: Jorge Jódar, Antonio González-Ramón, Sergio Martos-Rosillo, Javier Heredia, Christian Herrera, Javier Urrutia, Yván Caballero, Ane Zabaleta, Iñaki Antigüedad, Emilio Custodio, and Luis Javier Lambán

Supplementary material

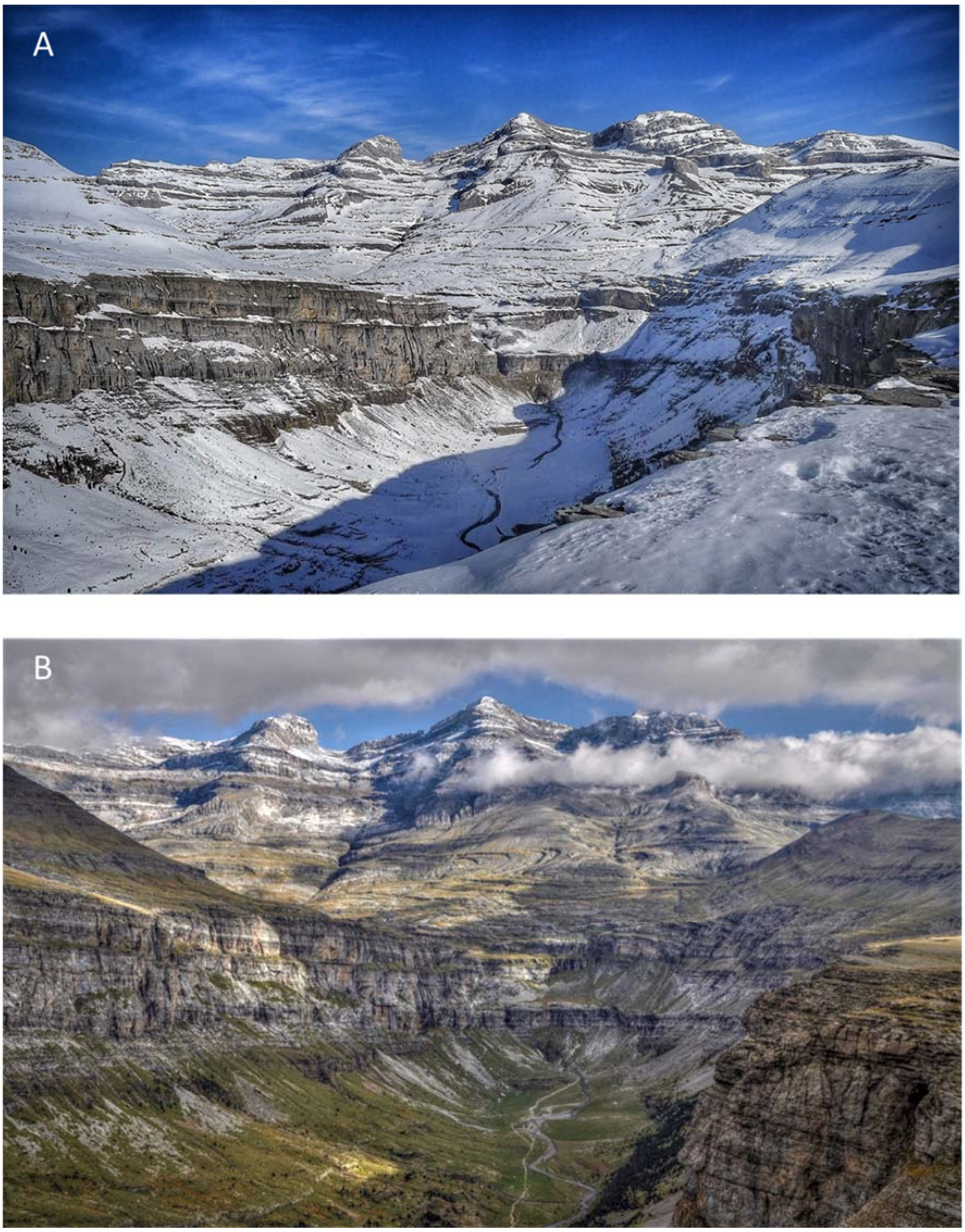

Fig. SM1. Views of the Soaso glacial cirque located in the upper Arazas River, and the Monte Perdido massif. (A) April 2019. (B) September 2019

Garcés Cave and Spring

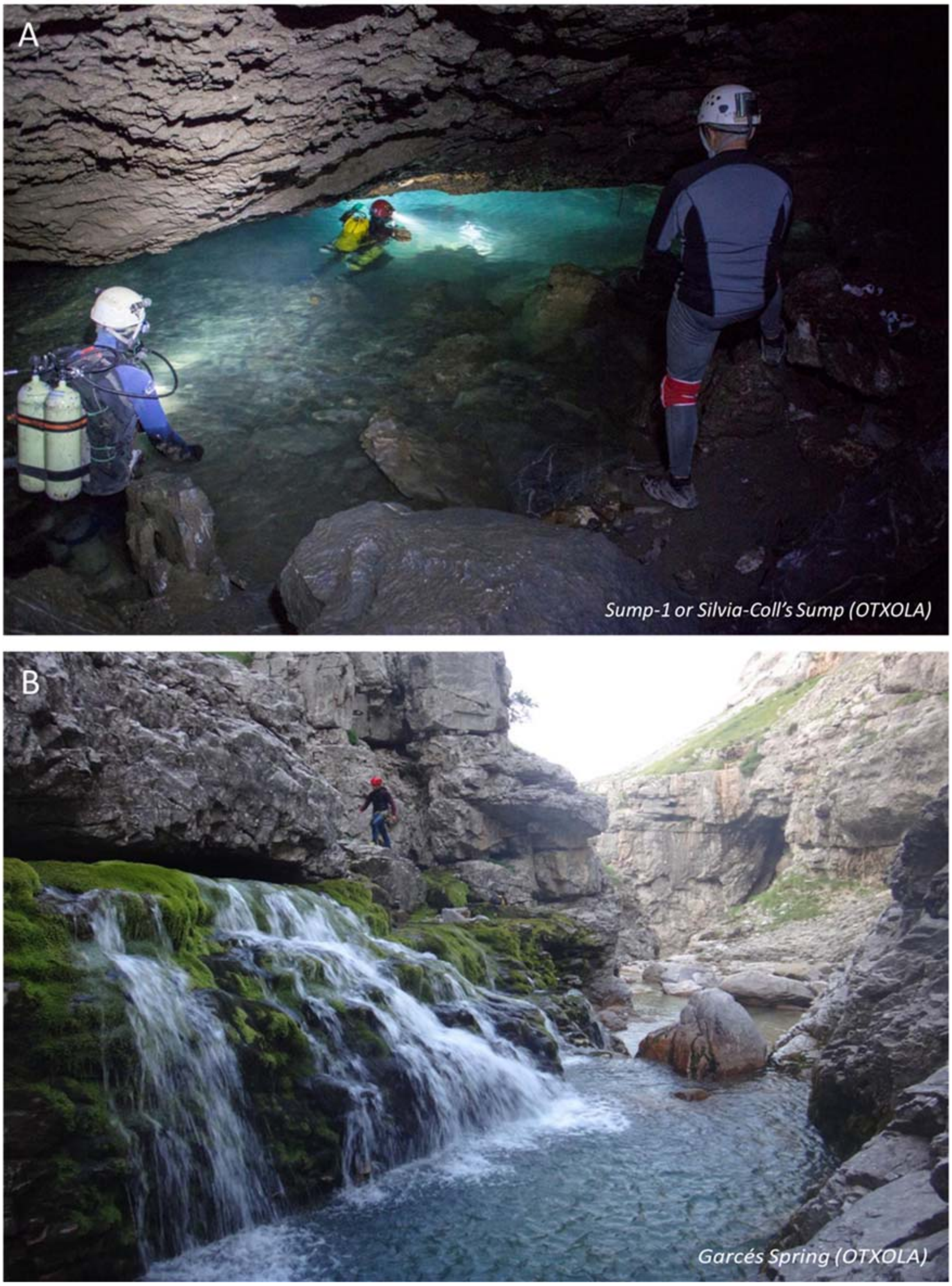

Fig. SM2. (A) Silvia-Coll's Sump in the Garcés Cave. (B) Gracés Spring

Cola de Caballo water fall

Fig. SM3. Cola de Caballo waterfall. (A) Nov.-2018, Chavier Lozano. (B) Mar.-2019. Aug.-2019, (D) Oct.-2019

Joints and fractures

Fig. SM4. Joints and fractures in the study area

Swallow-holes

Fig. SM5. Swallow-holes in the study area

Karst galleries

Fig. SM6. Galleries in the Garcés and Tartracina karst systems.